Article

Abrupt changes in biomass burning during the last glacial period

https://doi.org/10.1038/s41586-024-08363-3

Received: 5 April 2024

Accepted: 7 November 2024

Published online: 1 January 2025

Check for updates

Ben Riddell-Young[1,2]✉, James Edward Lee[3], Edward J. Brook[1], Jochen Schmitt[4], Hubertus Fischer[4], Thomas K. Bauska[5], James A. Menking[6], René Iseli[7] & Justin Reid Clark[8]

Understanding the causes of past atmospheric methane (CH_4) variability is important for characterizing the relationship between CH_4, global climate and terrestrial biogeochemical cycling. Ice core records of atmospheric CH_4 contain rapid variations linked to abrupt climate changes of the last glacial period known as Dansgaard–Oeschger (DO) events and Heinrich events (HE)[1,2]. The drivers of these CH_4 variations remain unknown but can be constrained with ice core measurements of the stable isotopic composition of atmospheric CH_4, which is sensitive to the strength of different isotopically distinguishable emission categories (microbial, pyrogenic and geologic)[3–5]. Here we present multi-decadal-scale measurements of $\delta^{13}C–CH_4$ and $\delta D–CH_4$ from the WAIS Divide and Talos Dome ice cores and identify abrupt 1‰ enrichments in $\delta^{13}C–CH_4$ synchronous with HE CH_4 pulses and 0.5‰ $\delta^{13}C–CH_4$ enrichments synchronous with DO CH_4 increases. $\delta D–CH_4$ varied little across the abrupt CH_4 changes. Using box models to interpret these isotopic shifts[6] and assuming a constant $\delta^{13}C–CH_4$ of microbial emissions, we propose that abrupt shifts in tropical rainfall associated with HEs and DO events enhanced ^{13}C-enriched pyrogenic CH_4 emissions, and by extension global wildfire extent, by 90–150%. Carbon cycle box modelling experiments[7] suggest that the resulting released terrestrial carbon could have caused from one-third to all of the abrupt CO_2 increases associated with HEs. These findings suggest that fire regimes and the terrestrial carbon cycle varied contemporaneously and substantially with past abrupt climate changes of the last glacial period.

Ice core measurements of atmospheric methane (CH_4) reveal its past variability. Identifying the causes of this variability is important for understanding global CH_4 biogeochemistry and its relation to climate. Because most CH_4 emissions originate from the terrestrial biosphere, drivers of past atmospheric variability can reveal the terrestrial biogeochemical and hydrologic components of past abrupt climate change at temporal scales not recorded by other proxies[1,2,8–10].

Rapid CH_4 changes of 50–150 ppb during the last glacial period (115–11.5 kyr) were contemporaneous with Dansgaard–Oeschger (DO) cycles[2,11], which are defined by abrupt, millennial-scale Northern Hemisphere (NH) temperature variations likely driven by rapid changes in Atlantic Meridional Overturning Circulation (AMOC) strength[12]. The warm phases of these cycles (DO interstadials) were associated with abrupt northward shifts of tropical rain belts and NH monsoon intensification[13,14], which likely enhanced microbial wetland CH_4 emissions[8,11,15].

Heinrich events (HEs) were extensive, multi-decadal-scale iceberg discharges into the North Atlantic Ocean that occasionally occurred within the stadial phase of DO cycles and considerably weakened AMOC[16], causing cascading impacts on the global climate system[7,17]. High-resolution speleothem records indicate both rapid drying of Asian Monsoon (ASM) regions[14] and Southern Hemisphere (SH) monsoon intensification[18] approximately coincident with HEs[14]. Multi-decadal-scale CH_4 pulses (about 50 ppb) have been linked to HEs, with proposed abrupt southward shifts of tropical rain belts enhancing southern tropical wetland CH_4 emissions[1,19]. However, quantitative constraints on the CH_4 budget across HEs and DO events are currently lacking.

Causes of past CH_4 variability can be investigated using measurements of the carbon and hydrogen stable isotopic composition of CH_4 ($\delta D–CH_4$ and $\delta^{13}C–CH_4$) (refs. 3–5). The three main emission categories—microbial (wetlands, ruminants and termites), pyrogenic (biomass burning, or BB) and geologic (marine clathrates, cold seepage and mud volcanoes)—have distinguishable isotopic compositions[4,5,20] (Extended Data Table 1). Changes in the proportion of these sources are reflected in the atmospheric isotopic composition. Specifically, $\delta D–CH_4$ and $\delta^{13}C–CH_4$ are both primarily influenced by the dominant, isotopically depleted microbial source, although $\delta^{13}C–CH_4$ is particularly sensitive to changes in ^{13}C-enriched pyrogenic emissions, whereas $\delta D–CH_4$ is strongly influenced by deuterium-enriched geologic emissions[4,5,20].

[1]College of Earth, Ocean, and Atmospheric Sciences (CEOAS), Oregon State University, Corvallis, OR, USA. [2]Cooperative Institute for Research in Environmental Sciences (CIRES), University of Colorado, Boulder, CO, USA. [3]Los Alamos National Laboratory, Los Alamos, NM, USA. [4]Climate and Environmental Physics, Physics Institute, and Oeschger Centre for Climate Change Research, University of Bern, Bern, Switzerland. [5]British Antarctic Survey, Cambridge, UK. [6]Commonwealth Scientific and Industrial Research Organization (CSIRO), Aspendale, Victoria, Australia. [7]Adolphe Merkle Institute, University of Fribourg, Fribourg, Switzerland. [8]Institute of Arctic and Alpine Research, University of Colorado, Boulder, CO, USA. ✉e-mail: Benjamin.riddell-young@noaa.gov

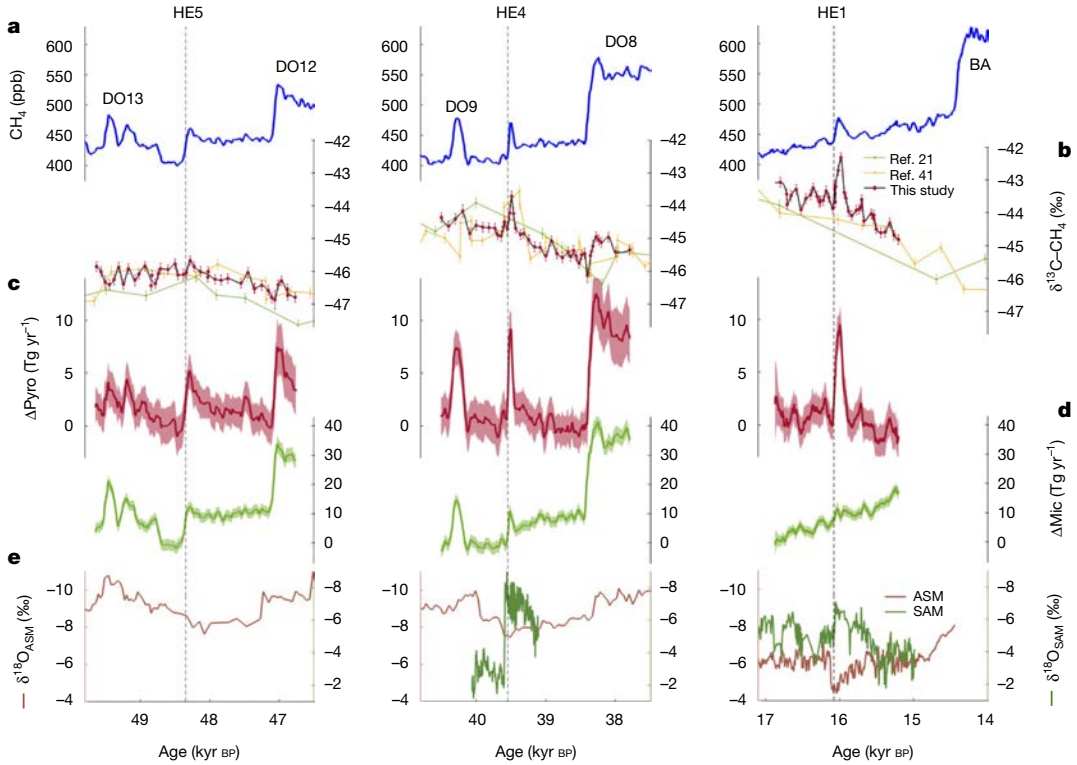

Fig. 1 | $\delta^{13}C$–CH_4 for HE5 and DO12, HE4 and DO8 and HE1. a, WDC CFA CH_4 data (blue)[39,53]. **b**, $\delta^{13}C$–CH_4 data from ref. 21 (green), ref. 41 (yellow) and this study (red diamonds, black line) each plotted with 1σ measurement uncertainties. **c**,**d**, Relative changes in pyrogenic (red) and microbial (green) emissions from the one-box model used to interpret the $\delta^{13}C$–CH_4 data. Shaded bands show Monte-Carlo-derived 95% confidence intervals related to analytical, firn diffusive, geologic emission and source signature uncertainties (Methods). **e**, $\delta^{18}O$–$CaCO_3$ records from speleothems in Asian Monsoon (ASM) (brown; HE4 and HE5, ref. 54; HE1, ref. 55) and South American Monsoon (SAM) regions (green; HE4, ref. 18; HE1, ref. 44). DO events and the Bölling Alleröd (BA) warming are labelled and HEs are indicated by vertical dashed lines. Note that the approximately 50 ppb CH_4 pulses discussed here are assumed synchronous with HEs[1].

The temporal resolution of existing Pleistocene $\delta^{13}C$–CH_4 records limits interpretations to multi-millennial timescales and existing δD–CH_4 data are limited[21]. Several records that used Greenland ice cores to increase data resolution across abrupt CH_4 changes[4,22] were likely contaminated by non-atmospheric CH_4 released during the analysis of dusty Greenland ice[23,24].

Abrupt CH_4 isotopic variations

We present multi-decadal-scale measurements across several prominent abrupt CH_4 changes associated with HEs and DO events using samples from Antarctic ice cores, which are not affected by non-atmospheric CH_4 contamination[23,24]. Specifically, we measured $\delta^{13}C$–CH_4 across the abrupt around 50 ppb CH_4 pulses associated with HE5, 4 and 1, and the abrupt 100–150 ppb CH_4 increases associated with DO12 and DO8 using ice from the WAIS Divide Ice Core (WDC) and WDC Replicate Core. WDC is ideal for high-resolution measurements because the high accumulation rates result in minimal smoothing of the gas record by firn processes (mean sample gas age distribution of 24–58 years) (ref. 9). Samples were also measured for δD–CH_4 using the WDC Replicate Core across the HE4 CH_4 pulse and the Talos Dome Ice Core (TALDICE) across DO8 (see Methods for detailed descriptions of sample measurement and data processing).

We identify hitherto undetected +1‰ $\delta^{13}C$–CH_4 anomalies synchronous with the abrupt CH_4 increases associated with HE4 and HE1 (ref. 1) and a smaller +0.5‰ anomaly across HE5 (Fig. 1b). During the larger CH_4 increases at the onset of DO12 and DO8, we observe +0.5‰ $\delta^{13}C$–CH_4 anomalies (Fig. 1b). Across the DO8 and HE4 CH_4 changes, δD–CH_4 varies little (Fig. 2e). To interpret these data, we used a one-box CH_4 stable isotope model[6,25] (equations (1–5)) and ran forward simulations using high-resolution continuous flow analysis (CFA) CH_4 data[1,9] and our interpolated $\delta^{13}C$–CH_4 data (Methods). The magnitude and $\delta^{13}C$–CH_4 of the global CH_4 source calculated from the model were used to determine the balance of pyrogenic and microbial emissions (equations (6) and (7) and Fig. 1c,d) using established source signatures (Extended Data Table 1) and assuming geologic emissions of 2.5 Tg yr^{-1} (1σ = 1.3 Tg yr^{-1}), as suggested by radiocarbon-derived constraints across deglacial abrupt CH_4 changes[10,26].

We tested our assumption of stable geologic emissions by comparing our DO8 and HE4 δD–CH_4 datasets with theoretical δD–CH_4 records generated using $\delta^{13}C$–CH_4-derived emissions that either assumed stable geologic emissions or stable pyrogenic emissions (Fig. 2e and Methods). The scenario in which deuterium-enriched geologic emissions[20] were allowed to vary while holding pyrogenic emissions constant caused substantial +15–20‰ δD–CH_4 anomalies at the HE4 and DO8 CH_4 increases (Fig. 2e). No such anomalies are observed in the WDC and TALDICE δD–CH_4 datasets. The theoretical δD–CH_4 record that assumed constant geologic emissions more closely matches the measured data (Fig. 2e). This supports radiocarbon-based evidence[10,26] that previously hypothesized marine CH_4 clathrate destabilization during abrupt DO interstadial warming[27] or HE iceberg discharge[28] did not occur at sufficient scale to impact atmospheric CH_4.

With geologic emissions assumed stable, $\delta^{13}C$–CH_4-derived pyrogenic emissions increased by 9–15 Tg yr^{-1} (+90–150% of annual pyrogenic CH_4 emissions) at the onset of each HE (Methods and Extended Data Table 2) and explain most of the CH_4 pulses across HEs (Fig. 1c). $\delta^{13}C$–CH_4-derived microbial emissions increase by about 10 Tg yr^{-1}

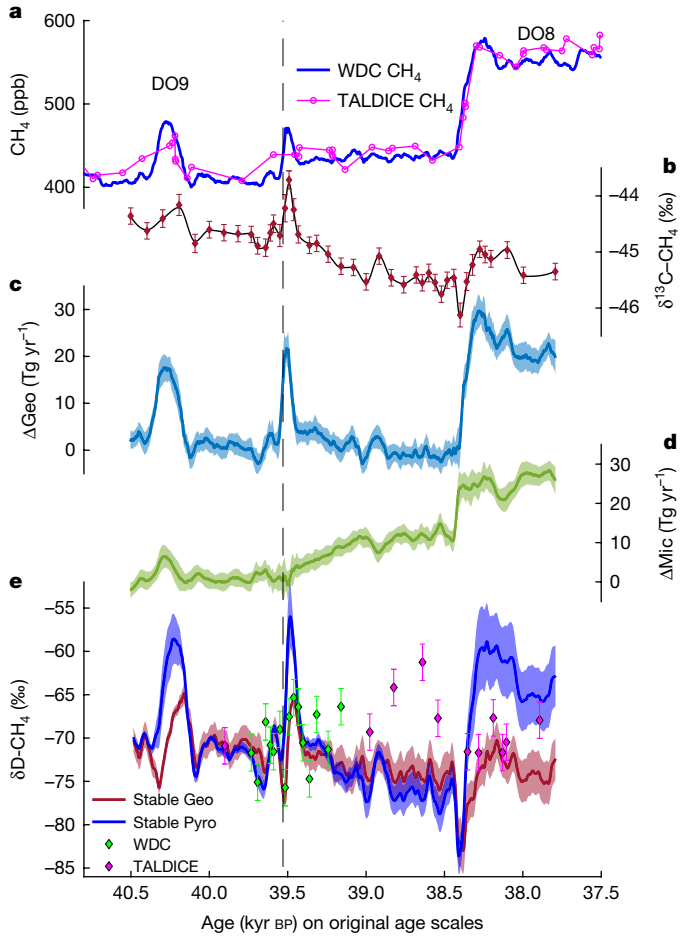

Fig. 2 | δD–CH_4 across HE4 and DO8. a, WDC CFA CH_4 data in blue[1,9], TALDICE CH_4 data in magenta[53] using the WDC-synchronized gas age scale from refs. 56,57. **b**, $\delta^{13}C$–CH_4 data from this study (red diamonds, black line) and 1σ measurement uncertainties. **c**,**d**, Relative changes in modelled geologic (light blue) and microbial (green) emissions assuming constant pyrogenic emissions. Shaded bands show Monte-Carlo-derived 95% confidence intervals related to analytical, firn diffusive and source signature uncertainties (Methods). **e**, Calculated theoretical δD–CH_4 using one-box model output for assumptions of constant geologic (red) and constant pyrogenic (dark blue) emissions. Measured δD–CH_4 and 1σ measurement uncertainties from WDC ice (this study, light green) and TALDICE (this study and ref. 58, magenta) plotted on the WDC-synchronized gas age scale from refs. 21,57. Shaded bands in **c**–**e** show Monte-Carlo-derived 95% confidence intervals related to analytical, firn diffusive and geologic emission and source signature uncertainties (Methods). DO interstadials are labelled and the onset of HE4 is indicated by a vertical dashed line.

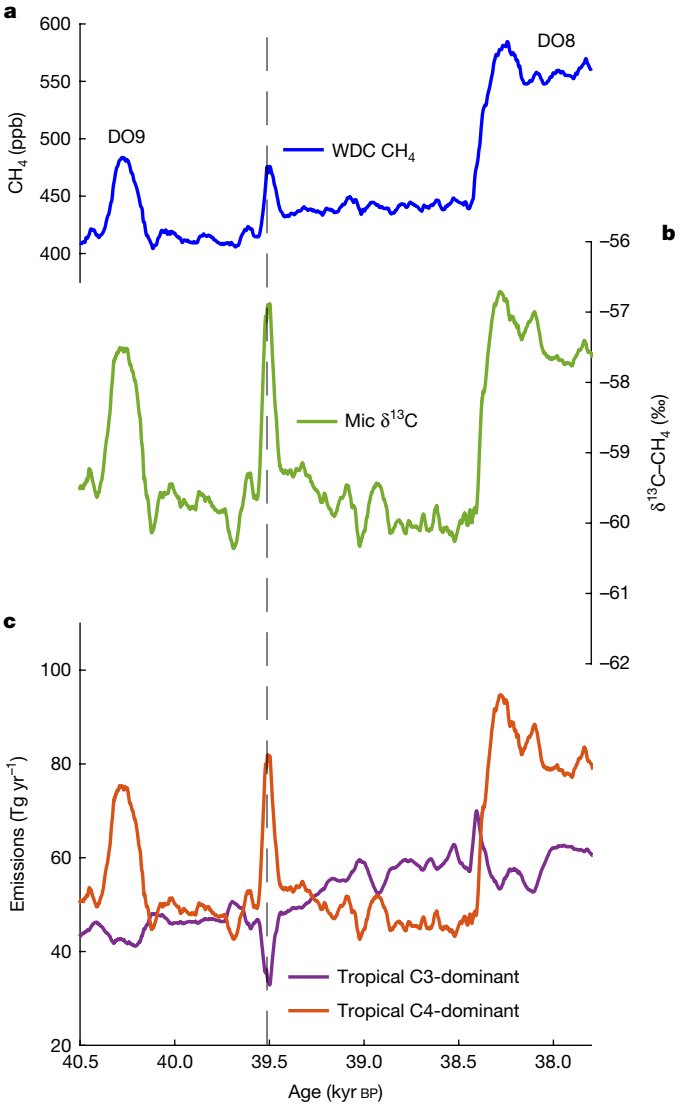

Fig. 3 | Sensitivity of analyses to variability in microbial $\delta^{13}C$–CH_4 across the HE4, DO8 interval. a, CFA CH_4 data[9,58] (blue). **b**, One-box-modelled microbial $\delta^{13}C$–CH_4 assuming constant pyrogenic and geologic $\delta^{13}C$–CH_4 and emissions. **c**, Changes in tropical microbial CH_4 emissions derived from C3-dominant (purple) or C4-dominant (orange) precursor biomass that are required to explain the observed atmospheric CH_4 and $\delta^{13}C$–CH_4 variability, assuming constant pyrogenic and geologic $\delta^{13}C$–CH_4 and emissions (**b**). DO interstadials are labelled and the onset of HE4 is indicated by a vertical dashed line.

to higher baselines across the HE5 and HE4 CH_4 pulses, suggesting a microbial driver of the observed elevated CH_4 after the pulses. Increasing background CH_4 surrounding HE1 is driven by a steady increase in modelled microbial emissions. The model primarily attributes the much larger abrupt CH_4 increases at the onsets of DO8 and DO12 to 20 Tg yr^{-1} and 30 Tg yr^{-1} increases in microbial emissions, respectively, but also suggests enhanced pyrogenic emissions comparable in magnitude to those modelled during HEs (Fig. 1c,d).

It is important to consider how variables other than changes to the proportion of emission categories might have contributed to observed atmospheric $\delta^{13}C$–CH_4 and δD–CH_4 variability. First, the relative contributions of different atmospheric CH_4 sinks, and thus sink fractionation, likely changed little across past abrupt CH_4 changes (Methods). Second, the Antarctic $\delta^{13}C$–CH_4 response to atmospheric CH_4 disequilibrium during times of rapid change (Extended Data Fig. 3) and the impact of latitudinal shifts in CH_4 emissions on the mean CH_4 age and thus isotopic composition of CH_4 reaching Antarctica (Extended Data Fig. 4) are both minimal relative to the observed $\delta^{13}C$–CH_4 variations (Methods). These effects are more pronounced for Antarctic δD–CH_4 because of stronger isotopic sink fractionation. Uncertainties associated with δD–CH_4 measurement precision[22], source signatures and sink fractionation[20,21] are also high. We therefore limit our interpretation of the δD–CH_4 datasets to exploring our assumption of stable geologic emissions, rather than use them to make quantitative constraints on the CH_4 budget.

More importantly, atmospheric $\delta^{13}C$–CH_4 is sensitive to changes in the $\delta^{13}C$–CH_4 of microbial emissions. For example, the $\delta^{13}C$–CH_4 of microbial and pyrogenic CH_4 emissions is partially determined by whether the precursor biomass is derived from C3 or C4 photosynthetic pathways[20], with C4-derived biomass 12‰ more enriched[29]. Precipitation changes related to HEs and DO events may have shifted the locations of tropical wetland CH_4 emissions to regions of differing vegetation type[13,30], affecting the magnitudes of C3- and C4-derived

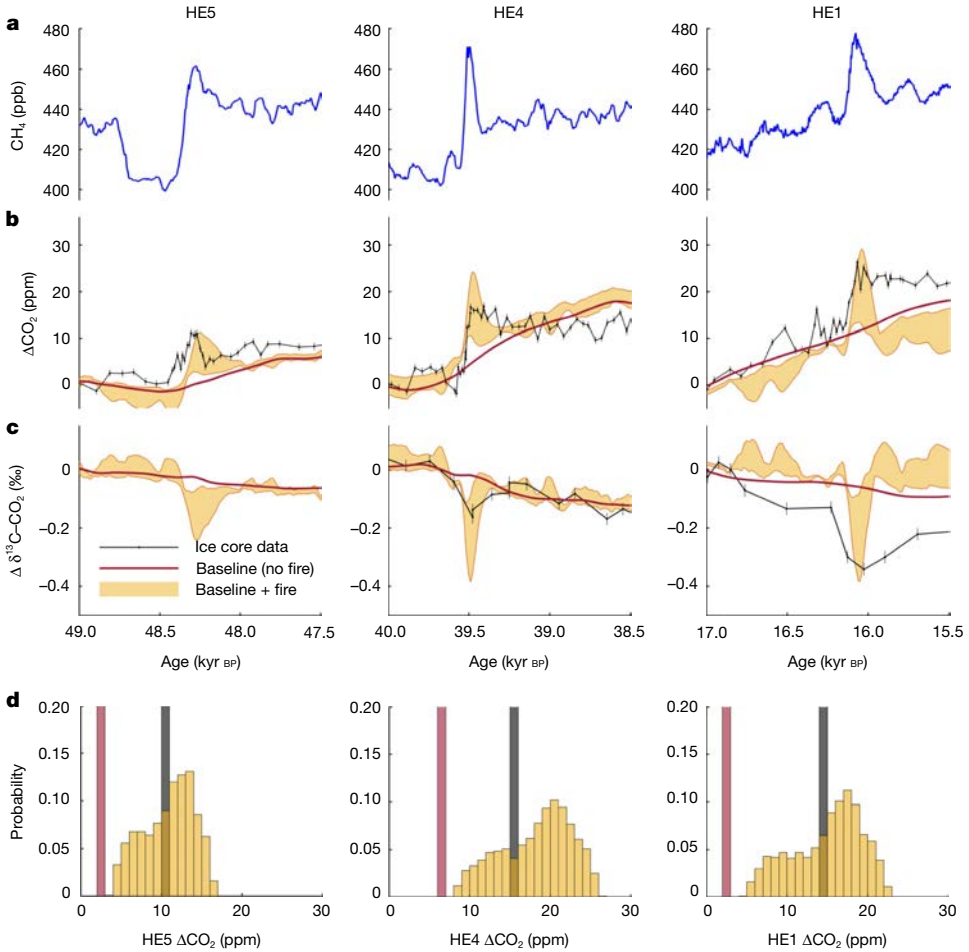

Fig. 4 | Modelled CO_2 across HE5, HE4 and HE1. a, WDC CFA CH_4 data (blue)[9,53]. **b**, Atmospheric CO_2 data and 1σ measurement uncertainties (WDC, black)[7,49,53,59], baseline carbon cycle box model output with stable terrestrial-atmosphere carbon flux (red) (model output from ref. 47), and the error envelope of the model output (95% confidence) including CO_2 fluxes related to pyrogenic emissions calculated using our CH_4 pyrogenic emissions (yellow shading). The error envelope was determined using a Monte Carlo error propagation related to uncertainties in pyrogenic CO_2 emissions and post-fire regrowth times (Methods). Data are plotted relative to CO_2 at the start of each interval. **c**, Same as **b** but for relative changes in $\delta^{13}C–CO_2$. Ice core $\delta^{13}C–CO_2$ data (plotted with 1σ measurement uncertainties) were measured using ice from Taylor Glacier (TG) and were shifted 150 years younger to match the WDC gas age scale[7]. **d**, Histogram showing the magnitude of CO_2 increase across each HE. Baseline model change (red)[49], WDC measured change (black) and Monte-Carlo-derived probability density function of the change of the baseline + pyrogenic results, which incorporates all uncertainties described in **b** (yellow).

microbial CH_4 emissions. Specifically, intensified methanogenesis in freshly inundated, C4-dominant regions might have caused the overshoots characteristic of the HE and DO event CH_4 increases[1]. Using our one-box model and equations (9) and (10) (Methods), we estimate that C3- and C4-derived microbial CH_4 emissions would need to have decreased by 35% and increased by 75% during HE4, respectively, to explain the observed CH_4 and $\delta^{13}C–CH_4$ change (Fig. 3). Similarly, a doubling of C4-derived microbial emissions would be required across the DO8 CH_4 increase.

These shifts in the C3–C4 balance of precursor biomass would have been quite substantial, but the palaeoecological evidence that allows examination of this scenario is limited and equivocal. Proxies of terrestrial precipitation[31] and paleo-vegetation models[32] suggest that the regions that experienced increased precipitation during HEs were both C3-dominant (Amazonia) and C4-dominant (Southern Africa and the Sunda/Sahul Shelves). Similarly, aridification occurred in regions composed of both C4 grasslands (Central Africa) and C3 forests (Eastern Asia)[31,32], highlighting the complexity of quantifying this effect. Although we cannot rule this mechanism, a change in pyrogenic emissions can plausibly explain our observations. Therefore, we hereafter explore the implications of this scenario, assuming constant microbial $\delta^{13}C–CH_4$ across HEs and DO events.

The terrestrial carbon cycle

The observation of comparable abrupt increases in pyrogenic CH_4 emissions across several HEs and DO events suggests that enhanced BB was a characteristic component of the carbon cycle during the abrupt climate variability of the last glacial period. We propose that during HEs, the southward displacement of tropical rain belts markedly dried regions of the NH tropics[14,33,34]. The resulting aridification of high biomass ecosystems in previously monsoon-influenced regions provided considerable fuel load for enhanced BB. The establishment of low fuel load ecosystems in the newly arid NH tropical environments[32,35] supports the modelled reduction of pyrogenic CH_4 emissions immediately following HEs (Fig. 1c). A microbial driver of elevated baseline CH_4 after HE5 and HE4 (Fig. 1d) is consistent with the evidence of enhanced precipitation and wetland expansion in SH tropical regions[1,13,34]. The microbial driver of increasing CH_4 surrounding HE1 was likely caused by rising global temperatures and the fertilization effects of increasing CO_2 during the last deglaciation[36].

Enhanced NH tropical BB during HEs is supported by proxy evidence of an abrupt onset of widespread Afro-Asian megadroughts during HE1 (refs. 33,37). Furthermore, a composite of charcoal records from Chinese Loess Plateau deposits indicates peak regional fire activity

contemporaneous with HE1 (ref. 38). The short duration of HEs limits terrestrial-based evidence of BB variability before HE1. Aerosol-based paleo-fire proxies in polar ice cores (for example, ammonia, formate and black carbon) do not record BB activity beyond polar and mid-latitude regions because of their short atmospheric residence times[39]. Ice core measurements of longer-lived atmospheric ethane and carbon monoxide offer more hemispheric integrations of BB[40] but records at sufficient precision and resolution have not yet been measured. Our $\delta^{13}C–CH_4$ data thus provide the first direct evidence of a global increase in BB during HEs.

Hypotheses of a dominant microbial driver of the CH_4 increases at the onset of DO12 and DO8 by enhanced NH tropical wetland emissions are consistent with our $\delta^{13}C–CH_4$ record and box model analyses[11,14,30,41]. The microbial CH_4 response to shifting precipitation was greater for DO events than for HEs because NH tropical regions contain greater land area conducive to wetland development[1,30]. This is in line with the proposed relationship between atmospheric CH_4 and global terrestrial ecosystem productivity[2,11,13,25]. These ecosystem and regional microbial CH_4 emission shifts are supported by records of the CH_4 interpolar difference[36], earth system modelling studies[15,42] and ASM speleothem records[14,34].

We link the increases in $\delta^{13}C–CH_4$-derived pyrogenic emissions at the onset of DO interstadials (Fig. 1c) to enhanced BB from both rapid drying in SH tropical regions[43,44] and increased NH vegetation cover that was susceptible to combustion during the dry season[39,45,46]. Evidence of enhanced BB during DO events is found in both global[46] and SH tropical[43] charcoal compilations. Similar to HEs, Chinese Loess Plateau charcoal records show enhanced BB contemporaneous with several late-glacial DO events[38]. Furthermore, more frequent ammonium deposition events in Greenland during DO events have been linked to increased North American BB[39,46].

The significant increases in pyrogenic CH_4 emissions during both HEs and DO events suggest major and abrupt changes to global ecosystem structure, terrestrial biogeochemistry and carbon cycling. Rapid atmospheric CO_2 increases of up to 15 ppm have been linked to HEs and were contemporaneous with the abrupt CH_4 pulses[7,47,48]. Ice core records of atmospheric $\delta^{13}C–CO_2$ show abrupt isotopic depletion synchronous with the HE1 and HE4 CO_2 increases, suggesting organic carbon of terrestrial or marine origin[7,49]. An oceanic source has received the most attention, with compelling, although resolution-limited, evidence of rapid Southern Ocean overturning of CO_2-rich deep water that abruptly outgassed and increased atmospheric CO_2 (refs. 48,50). Our $\delta^{13}C–CH_4$ record and calculated pyrogenic emissions provide evidence of an important terrestrial CO_2 source.

We explore this possibility using a 14-box, isotope-enabled ocean, atmosphere and terrestrial biosphere carbon cycle model that is forced by proxies of ocean circulation and climate derived from ocean sediments and ice cores[49] (Methods) to quantify the impact of enhanced pyrogenic emissions on atmospheric CO_2. Previously, with terrestrial carbon exchange held constant, the model captured glacial-interglacial and millennial-scale CO_2 and $\delta^{13}C–CO_2$ variability by Southern Ocean mechanisms with comparable accuracy to state-of-the-art carbon cycle models but failed to reproduce the abrupt changes related to HEs[7]. Here, we varied terrestrial carbon fluxes using our $\delta^{13}C–CH_4$-derived pyrogenic CH_4 emissions and modern CO_2-to-CH_4 emission ratios to calculate global pyrogenic CO_2 emissions and eventual post-fire regrowth (Methods). The resulting time series was then input into the model as a terrestrial carbon flux to the atmosphere.

Including our estimates of pyrogenic CO_2 emissions markedly improves the agreement of the model with CO_2 and $\delta^{13}C–CO_2$ across HEs (Fig. 4). We estimate that enhanced BB contributed to 5–15 ppm (33–100%) of the abrupt CO_2 increases associated with HE5, 4, and 1 and that these BB events combusted an additional 285–637 million hectares per year at their peak; equivalent to 1/2 to roughly all of modern annual global burned area (Methods). Shortcomings of the model are exemplified by overestimates of the smaller abrupt CO_2 increases at DO interstadial onsets[47]. This disagreement could stem from the assumption of the model of stable terrestrial carbon reservoirs outside of changes associated with BB. Increased NH tropical vegetation cover during DO interstadials[30,32,45] is not captured in the model but would offset the carbon released from enhanced BB (Methods and Extended Data Fig. 5). We propose that this offsetting effect was minimal during stadial intervals when terrestrial carbon accumulation was probably minor and limited to the SH tropics, as suggested by several paleo-ecological modelling studies[32,51].

The agreement between modelled and observed CO_2 and $\delta^{13}C–CO_2$ across HEs suggests that our $\delta^{13}C–CH_4$ data and CH_4 model output provide plausible estimates of changes to the CH_4 budget and global BB. Furthermore, our data offer empirical evidence that the terrestrial biosphere played a key part in multi-decadal-scale CO_2 increases associated with HEs, although we cannot rule out an important oceanic contribution[48]. Vegetation-coupled earth system models have been run to equilibrium in climate states with both active and collapsed AMOC to simulate the response of terrestrial carbon to HEs[30,32,51,52]. The resulting net terrestrial carbon loss (28–91 Pg) (ref. 32) is comparable to the loss implied by our modelled transient excess pyrogenic carbon emissions (43–146 Pg), suggesting that our estimates are reasonable. Our time series may provide a valuable comparison for future paleo-ecological studies that simulate the transient response of the terrestrial biosphere to HEs. The findings of this study show that global fire regimes varied contemporaneously and substantially with past climate changes over very short time periods and reveal a new mechanistic relationship between CH_4 and CO_2, the terrestrial carbon cycle and abrupt climate change.

Online content

Any methods, additional references, Nature Portfolio reporting summaries, source data, extended data, supplementary information, acknowledgements, peer review information; details of author contributions and competing interests; and statements of data and code availability are available at https://doi.org/10.1038/s41586-024-08363-3.

1. Rhodes, R. H. et al. Enhanced tropical methane production in response to iceberg discharge in the North Atlantic. *Science* **348**, 1016–1019 (2015).
2. Brook, E. J., Sowers, T. & Orchardo, J. Rapid variations in atmospheric methane concentration during the past 110,000 years. *Science* **273**, 1087–1091 (1996).
3. Ferretti, D. et al. Unexpected changes to the global methane budget over the past 2000 years. *Science* **309**, 1714–1717 (2005).
4. Sowers, T. Late quaternary atmospheric CH_4 isotope record suggests marine clathrates are stable. *Science* **311**, 838–840 (2006).
5. Fischer, H. et al. Changing boreal methane sources and constant biomass burning during the last termination. *Nature* **452**, 864–867 (2008).
6. Tans, P. P. A note on isotopic ratios and the global atmospheric methane budget. *Global Biogeochem. Cycles* **11**, 77–81 (1997).
7. Bauska, T. K., Marcott, S. A. & Brook, E. J. Abrupt changes in the global carbon cycle during the last glacial period. *Nat. Geosci.* **14**, 91–96 (2021).
8. Chappellaz, J. et al. Synchronous changes in atmospheric CH_4 and Greenland climate between 40 and 8 kyrBP. *Nature* **366**, 443–445 (1993).
9. Rhodes, R. H. et al. Atmospheric methane variability: centennial-scale signals in the Last Glacial Period. *Global Biogeochem. Cycles* **31**, 575–590 (2017).
10. Dyonisius, M. et al. Old carbon reservoirs were not important in the deglacial methane budget. *Science* **367**, 907–910 (2020).
11. Brook, E. J., Harder, S., Severinghaus, J., Steig, E. J. & Sucher, C. M. On the origin and timing of rapid changes in atmospheric methane during the last glacial period. *Global Biogeochem. Cycles* **14**, 559–572 (2000).
12. Dansgaard, W. et al. A new Greenland deep ice core. *Science* **218**, 1273–1277 (1982).
13. Seltzer, A. M. et al. Does $\delta^{18}O$ of O_2 record meridional shifts in tropical rainfall? *Clim. Past* **13**, 1323–1338 (2017).
14. Deplazes, G. et al. Weakening and strengthening of the Indian monsoon during Heinrich events and Dansgaard-Oeschger oscillations. *Paleoceanography* **29**, 99–114 (2014).
15. Hopcroft, P. O., Valdes, P. J., O'Connor, F. M., Kaplan, J. O. & Beerling, D. J. Understanding the glacial methane cycle. *Nat. Commun.* **8**, 14383 (2017).
16. Heinrich, H. Origin and consequences of cyclic ice rafting in the northeast Atlantic Ocean during the past 130,000 years. *Quat. Res.* **29**, 142–152 (1988).
17. Hemming, S. R. Heinrich events: massive late Pleistocene detritus layers of the North Atlantic and their global climate imprint. *Rev. Geophys.* **42**, RG1005 (2004).
18. Wendt, K. A. et al. Three-phased Heinrich Stadial 4 recorded in NE Brazil stalagmites. *Earth Planet. Sci. Lett.* **510**, 94–102 (2019).

19. Martin, K. C. et al. Bipolar impact and phasing of Heinrich-type climate variability. *Nature* **617**, 100–104 (2023).
20. Sherwood, O. A., Schwietzke, S., Arling, V. A. & Etiope, G. Global inventory of gas geochemistry data from fossil fuel, microbial and burning sources, version 2017. *Earth Syst. Sci. Data* **9**, 639–656 (2017).
21. Bock, M. et al. Glacial/interglacial wetland, biomass burning, and geologic methane emissions constrained by dual stable isotopic CH4 ice core records. *Proc. Natl Acad. Sci. USA* **114**, E5778–E5786 (2017).
22. Bock, M. et al. A gas chromatography/pyrolysis/isotope ratio mass spectrometry system for high-precision δD measurements of atmospheric methane extracted from ice cores. *Rapid Commun. Mass Spectrom.* **24**, 621–633 (2010).
23. Lee, J. E. et al. Excess methane in Greenland ice cores associated with high dust concentrations. *Geochim. Cosmochim. Acta* **270**, 409–430 (2020).
24. Mühl, M. et al. Methane, ethane, and propane production in Greenland ice core samples and a first isotopic characterization of excess methane. *Clim. Past* **19**, 999–1025 (2023).
25. Chappellaz, J., Barnola, J. M., Raynaud, D., Korotkevich, Y. S. & Lorius, C. Ice-core record of atmospheric methane over the past 160,000 years. *Nature* **345**, 127–131 (1990).
26. Petrenko, V. V. et al. Minimal geological methane emissions during the Younger Dryas–Preboreal abrupt warming event. *Nature* **548**, 443–446 (2017).
27. Kennett, J. P., Cannariato, K. G., Hendy, I. L. & Behl, R. J. Carbon isotopic evidence for methane hydrate instability during Quaternary interstadials. *Science* **288**, 128–133 (2000).
28. Flückiger, J., Knutti, R. & White, J. W. C. Oceanic processes as potential trigger and amplifying mechanisms for Heinrich events. *Paleoceanography* **21**, PA2014 (2006).
29. Ganesan, A. L. et al. Spatially resolved isotopic source signatures of wetland methane emissions. *Geophys. Res. Lett.* **45**, 3737–3745 (2018).
30. Hopcroft, P. O., Valdes, P. J. & Beerling, D. J. Simulating idealized Dansgaard-Oeschger events and their potential impacts on the global methane cycle. *Quat. Sci. Rev.* **30**, 3258–3268 (2011).
31. Bradley, R. S. & Diaz, H. F. Late quaternary abrupt climate change in the tropics and sub-tropics: the continental signal of tropical hydroclimatic events (THEs). *Rev. Geophys.* **59**, e2020RG000732 (2021).
32. Allen, J. R. et al. Global vegetation patterns of the past 140,000 years. *J. Biogeogr.* **47**, 2073–2090 (2020).
33. Itambi, A. C., von Dobeneck, T., Mulitza, S., Bickert, T. & Heslop, D. Millennial-scale northwest African droughts related to Heinrich events and Dansgaard-Oeschger cycles: evidence in marine sediments from offshore Senegal. *Paleoceanography* **24**, PA1205 (2009).
34. Scroxton, N. et al. Antiphase response of the Indonesian–Australian monsoon to millennial-scale events of the last glacial period. *Sci. Rep.* **12**, 20214 (2022).
35. Niu, D. et al. C_4 vegetation characteristics in the monsoon rainforest of the Pearl River delta during the MIS 2 period. *Org. Geochem.* **173**, 104494 (2022).
36. Riddell-Young, B. et al. Atmospheric methane variability through the Last Glacial Maximum and deglaciation mainly controlled by tropical sources. *Nat. Geosci.* **16**, 1174–1180 (2023).
37. Zhou, X. et al. Catastrophic drought in East Asian monsoon region during Heinrich event 1. *Quat. Sci. Rev.* **141**, 1–8 (2016).
38. Wang, X., Ding, Z., & Peng, P. Changes in fire regimes on the Chinese Loess Plateau since the last glacial maximum and implications for linkages to paleoclimate and past human activity. *Palaeogeogr. Palaeoclimatol. Palaeoecol.* **315**, 61–74 (2012).
39. Fischer, H. et al. Millennial changes in North American wildfire and soil activity over the last glacial cycle. *Nat. Geosci.* **8**, 723–727 (2015).
40. Nicewonger, M. R., Aydin, M., Prather, M. J. & Saltzman, E. S. Extracting a history of global fire emissions for the past millennium from ice core records of acetylene, ethane, and methane. *J. Geophys. Res. Atmos.* **125**, e2020JD032932 (2020).
41. Möller, L. et al. Independent variations of CH_4 emissions and isotopic composition over the past 160,000 years. *Nat. Geosci.* **6**, 885–890 (2013).
42. Kleinen, T., Gromov, S., Steil, B. & Brovkin, V. Atmospheric methane since the last glacial maximum was driven by wetland sources. *Clim. Past* **19**, 1081–1099 (2023).
43. Mooney, S. D. et al. Late Quaternary fire regimes of Australasia. *Quat. Sci. Rev.* **30**, 28–46 (2011).
44. Stríkis, N. M. et al. South American monsoon response to iceberg discharge in the North Atlantic. *Proc. Natl Acad. Sci. USA* **115**, 3788–3793 (2018).
45. Harrison, S. & Goñi, M. S. Global patterns of vegetation response to millennial-scale variability and rapid climate change during the last glacial period. *Quat. Sci. Rev.* **29**, 2957–2980 (2010).
46. Daniau, A.-L., Harrison, S. & Bartlein, P. Fire regimes during the Last Glacial. *Quat. Sci. Rev.* **29**, 2918–2930 (2010).
47. Marcott, S. A. et al. Centennial-scale changes in the global carbon cycle during the last deglaciation. *Nature* **514**, 616–619 (2014).
48. Menviel, L. et al. Southern Hemisphere westerlies as a driver of the early deglacial atmospheric CO_2 rise. *Nat. Commun.* **9**, 2503 (2018).
49. Bauska, T. K. et al. Carbon isotopes characterize rapid changes in atmospheric carbon dioxide during the last deglaciation. *Proc. Natl Acad. Sci. USA* **113**, 3465–3470 (2016).
50. Rae, J. W. et al. CO_2 storage and release in the deep Southern Ocean on millennial to centennial timescales. *Nature* **562**, 569–573 (2018).
51. Nielsen, S. B., Jochum, M., Pedro, J. B., Eden, C. & Nuterman, R. Two-timescale carbon cycle response to an AMOC collapse. *Paleoceanogr. Paleoclimatol.* **34**, 511–523 (2019).
52. Bozbiyik, A., Steinacher, M., Joos, F., Stocker, T. F. & Menviel, L. Fingerprints of changes in the terrestrial carbon cycle in response to large reorganizations in ocean circulation. *Clim. Past* **7**, 319–338 (2011).
53. Buizert, C. et al. The WAIS Divide Deep Ice Core WD2014 chronology – Part 1: methane synchronization (68–31 ka BP) and the gas age–ice age difference. *Clim. Past* **11**, 153–173 (2015).
54. Cheng, H. et al. The Asian monsoon over the past 640,000 years and ice age terminations. *Nature* **534**, 640–646 (2016).
55. Zhang, W. et al. A detailed East Asian monsoon history surrounding the 'Mystery Interval' derived from three Chinese speleothem records. *Quat. Res.* **82**, 154–163 (2014).
56. Buiron, D. et al. TALDICE-1 age scale of the Talos Dome Deep Ice Core, East Antarctica. *Clim. Past* **7**, 1–16 (2011).
57. Buizert, C. et al. Abrupt ice-age shifts in southern westerly winds and Antarctic climate forced from the north. *Nature* **563**, 681–685 (2018).
58. Buizert, C. et al. Antarctic surface temperature and elevation during the Last Glacial Maximum. *Science* **372**, 1097–1101 (2021).
59. Wendt, K. A. et al. Southern Ocean drives multidecadal atmospheric CO_2 rise during Heinrich Stadials. *Proc. Natl Acad. Sci. USA* **121**, e2319652121 (2024).

Methods

Ice core measurements

The ice core CH_4 stable isotope data presented in this study were measured using analytical systems at the University of Bern[22,60,61] and Oregon State University (OSU). The OSU system is modelled after the Bern system and consists of an extraction line for separating CH_4 from other air components and measuring the total amount of air in the sample, a combustion system to produce CO_2 from CH_4 (Thermo GC-IsoLink) and a Thermo Delta V mass spectrometer configured to measure $\delta^{13}C$–CO_2 (for further details, see Extended Data Fig. 6 and Supplementary Information section 1).

The pooled standard deviation of replicate $\delta^{13}C$–CH_4 measurements is comparable between the OSU system (1σ = 0.14‰ for 250 g samples) and the Bern system (1σ = 0.15‰ for 150 g samples)[60]. For δD–CH_4, Bern reports a 1σ precision of 2.1‰ for 300 g samples[22,61]. Both systems are calibrated to the VPDB-CO_2 scale (Supplementary Information section 2).

On the OSU system, WDC samples were measured for $\delta^{13}C$–CH_4 across HE5 and DO12 from 49.6 kyr to 46.8 kyr (43 samples at 67-year mean resolution) and HE1 from 17.0 kyr to 15.3 kyr (41 samples at 40-year mean resolution). The Bern system was used to measure ice samples from the WAIS Divide Replicate Core[62,63], covering HE4 and DO8 for both $\delta^{13}C$–CH_4 (40.5–37.8 kyr; 43 samples at 63-year mean resolution) and δD-CH_4 (39.7–39.2 kyr; 15 samples at 38-year mean resolution). The WAIS Divide Replicate Core is offset in depth from WDC by 0.7375 m for the depth range we analysed. Finally, 11 samples from TALDICE were measured for δD–CH_4 across the DO8 transition on the Bern system, with a mean resolution of 110 years. The TALDICE gas age scale from refs. 57,58 was used to synchronize the TALDICE record to the WDC gas age scale (Fig. 2a,e). Although these HEs and DO events were prioritized because of their prominence and the notable labour involved in measurements, future studies should investigate other abrupt CH_4 changes to better define the recurrence of our observed isotopic anomalies.

The measured $\delta^{13}C$–CH_4 in ice core samples must be corrected for fractionation in the porous firn column. First, gravitational fractionation enriches the bottom of the firn column with $^{13}CH_4$ (ref. 64). This effect is quantified using $\delta^{15}N$–N_2 measurements[64,65], which have been made at high resolution in WDC samples[53]. The gravitational fractionation correction based on $\delta^{15}N$–N_2 is about 0.3‰ in WDC. Second, $^{13}CH_4$ and $^{12}CH_4$ diffuse at different rates, causing a diffusive fractionation when concentration gradients are present in the firn, for example, at times of abrupt atmospheric CH_4 change. This effect was corrected for by using the methods described in ref. 66. The high-resolution of WDC CFA CH_4 data[1] provides robust quantifications of this effect across the abrupt CH_4 change investigated in this study. The CFA data were first smoothed using a Gaussian smoothing window of 20 years to dampen analytical noise that caused unrealistic estimates of instantaneous rates of CH_4 change. The diffusive column height and gas age at lock-in, two variables needed to calculate diffusive fractionation, were both determined using $\delta^{15}N$–N_2 (refs. 66,67). We find that, during the intervals of the most rapid CH_4 change, diffusive fractionation imparts a maximum −0.8‰ anomaly on the $\delta^{13}C$–CH_4 signal trapped in the ice, highlighting the importance of these corrections. However, the measured positive anomalies in $\delta^{13}C$–CH_4 are observable in data both corrected and not corrected for diffusive fractionation and are thus not dependent on the accuracy of this correction (Extended Data Fig. 1). The WDC and TALDICE δD–CH_4 data were also corrected for gravitational and diffusive fractionation using $\delta^{15}N$–N_2 (refs. 56,66,67), although these effects are small relative to δD measurement precision and signal amplitude.

The 1σ total uncertainties for each measurement were calculated by propagating uncertainties associated with gravitational fractionation (0.04‰), diffusive fractionation (30% of the calculated value[66]) and analytical error (0.14‰). The largest uncertainties (0.24‰) occur during intervals of abrupt CH_4 change when diffusive fractionation is the greatest but do not limit conclusive interpretations of the data.

Box model analyses

To interpret our CH_4 stable isotope data, we used a one-box model[6]. These models are advantageous because they offer a simplified yet well-constrained framework for understanding complex CH_4 biogeochemistry[68,69]. We first averaged replicate samples and interpolated our $\delta^{13}C$–CH_4 record to match the resolution of the 20-year Gaussian-smoothed WDC CH_4 CFA data. Latitudinal gradients in CH_4 (the Interpolar Difference, or IPD) and $\delta^{13}C$–CH_4 may have existed during the investigated time intervals[11,36,70,71]. However, owing to limited IPD measurements and centennial-scale uncertainties[36], we assume a stable IPD at 2% of total atmospheric CH_4 (refs. 11,36,70) and multiply the WDC CH_4 record by a factor of 1.01 to estimate the global mean burden. This assumption is not impactful to our interpretations of the CH_4 budget. Two-box model sensitivity tests (see below) indicate that Antarctic $\delta^{13}C$–CH_4 was minimally affected by possible past IPD variability[36] (Extended Data Fig. 4). The smoothed CH_4 record was then used to calculate the total source ($^{12}CH_4$ + $^{13}CH_4$) by solving for S in equation (1):

$$\frac{dX_n}{dt} = S - \frac{X_n}{L} \quad (1)$$

where S is the annual global CH_4 source (Tg yr^{-1}), L is the atmospheric lifetime (9 years) (ref. 72) and X is the atmospheric CH_4 burden (Tg of all isotopologues) at timestep n, calculated using the following mass balance:

$$X = \frac{M_A}{MM_A} \times \frac{CFA \times 1.01}{10^9} \times \frac{MM_{CH4}}{10^{12}} \quad (2)$$

where M_A is the mass of the atmosphere (5.15×10^{21} g), MM_A is the molar mass of the atmosphere (28.97 g mol^{-1}), CFA is the smoothed Antarctic CH_4 CFA record and MM_{CH4} is the molar mass of CH_4 (16.04 g mol^{-1}). Equation (1) can be modified to calculate the $^{13}CH_4$ source (S^{13C}) at each timestep:

$$\frac{dX_n^{13C}}{dt} = S^{13C} - \frac{X_n^{13C}}{L} \times \alpha \quad (3)$$

where X^{13C} refers to the atmospheric $^{13}CH_4$ burden and α is the kinetic fractionation factor of the combined effect of all CH_4 sinks (reaction with OH, chlorine and soil oxidation; 0.994) (refs. 73,74). Changes in the relative contributions of different sinks could affect $\delta^{13}C$–CH_4 and δD–CH_4. For example, increased mineral dust interaction with sea salt aerosols during stadial intervals could have increased the chlorine sink[75], causing stronger sink fractionation and $\delta^{13}C$–CH_4 enrichment. This may explain some of the multi-millennial-scale $\delta^{13}C$–CH_4 variability identified in refs. 21,41. Although low-latitude dust archives lack multi-decadal-scale resolution, the abrupt CH_4 pulses and $\delta^{13}C$–CH_4 anomalies are not accompanied by pulses of mineral dust and sea salt aerosol in Greenland and Antarctic ice cores[19,76,77]. We, therefore, assume that the chlorine sink, lifetime and sink fractionation were stable over the short intervals investigated in this study[72].

The $^{13}CH_4$ atmospheric burden, or X^{13C} in equation (3), is calculated from our measured, interpolated atmospheric $\delta^{13}C$–CH_4 record ($\delta^{13}C$) using equation (4):

$$X^{13C} = \left(\frac{\delta^{13}C}{1{,}000} + 1\right) \times R_{std} \times X \quad (4)$$

where R_{std} is the VPDB standard for $\frac{^{13}C}{^{13}C + ^{12}C}$. We then calculate the $\delta^{13}C$–CH_4 of the global CH_4 source ($\delta^{13}C_S$) using equation (5):

$$\delta^{13}C_S = \left(\frac{R_S^{13C}}{R_{std}} - 1\right) \times 1{,}000 \quad (5)$$

where R_S^{13C} is the $\frac{^{13}C}{^{13}C + ^{12}C}$, or $\frac{S^{13C}}{S}$, of the global CH_4 source. With the strength (S) and $\delta^{13}C$–CH_4 ($\delta^{13}C$) of the global CH_4 source known, the following isotope mass balance system of equations can be used to estimate microbial (Mic), geologic (Geo) and pyrogenic (Pyro) emissions:

$$S = S_{Mic} + S_{Pyro} + S_{Geo} \quad (6)$$

$$S \times \delta^{13}C_S = S_{Mic} \times \delta^{13}C_{Mic} + S_{Pyro} \times \delta^{13}C_{Pyro} + S_{Geo} \times \delta^{13}C_{Geo} \quad (7)$$

where the subscripts denote each emission type (Extended Data Table 1). Solving the system of equations, we obtain estimates of pyrogenic and microbial emissions in Tg yr^{-1} (Fig. 1c,d) assuming geologic emissions of 2.5 Tg yr^{-1} (1σ = 1.3 Tg yr^{-1}).

The total uncertainty of each measurement is incorporated into our box model using a 10,000-iteration Monte Carlo approach. Because our interpretations primarily focus on relative changes to the CH_4 budget over time, and because we assume stable $\delta^{13}C$-CH_4 of major sources over multi-decadal timescales, we show emission estimates as relative change over time (Figs. 1 and 2). This enables us to isolate uncertainties in the global CH_4 budget from uncertainties in how the budget changes over time.

To explore our assumption of stable geologic emissions, the magnitudes of emission types were calculated for two scenarios using equations (6) and (7) by assuming both stable geologic and pyrogenic emissions. Equation (8) (see Extended Data Table 1 for source signatures)[21] was then used to estimate the δD-CH_4 of the total source (δD_S):

$$S \times \delta D_S = S_{Mic} \times \delta D_{Mic} + S_{Pyro} \times \delta D_{Pyro} + S_{Geo} \times \delta D_{Geo} \quad (8)$$

The resulting time series of S and δD_S were then used with δD-enabled versions of equations (1–5) (α = 0.7634) (refs. 73,78) to calculate atmospheric δD–CH_4 for the HE4–DO8 interval for both emission scenarios (Fig. 2). Under stable pyrogenic emissions, δD–CH_4 would have experienced +15–20‰ anomalies across HE4 and DO8 that were driven by enhanced geologic emissions. These anomalies could have been larger if previously proposed marine clathrate destabilization[27,28] drove the CH_4 increases due to isotopic enrichments during water column oxidation before atmospheric release[79,80].

Sensitivity tests

Changes in source CH_4 isotopic signature. To quantify how much microbial $\delta^{13}C$–CH_4 would need to have changed to cause the observed CH_4 and $\delta^{13}C$–CH_4 variability across HE4 and the onset of DO8, we assumed constant pyrogenic and geologic emissions and solved equations (6) and (7) for S_{Mic} and $\delta^{13}C_{Mic}$. We estimate that abrupt roughly 4‰ enrichments in $\delta^{13}C_{Mic}$ would be required across both abrupt CH_4 increases (Fig. 3b). This shift could only occur through a marked change in the C3:C4 ratio of methanogenesis precursor biomass. We established a new isotope mass balance to determine C3- and C4-dominant components of microbial emissions (see Extended Data Table 1 for source signatures):

$$S_{Mic} = S_{HL} + S_{C3} + S_{C4} \quad (9)$$

$$S_{Mic} \times \delta^{13}C_{Mic} = S_{HL} \times \delta^{13}C_{HL} + S_{C3} \times \delta^{13}C_{C3} + S_{C4} \times \delta^{13}C_{C4} \quad (10)$$

where S_{HL} is the strength of high-latitude NH microbial emissions (assumed stable at 10 Tg yr^{-1}) (ref. 10). The results (Fig. 3c and Extended Data Fig. 2) are minimally sensitive to the assumed strengths of high-latitude NH microbial, geologic and pyrogenic emissions. Using similar methods, we find that the scenario in which only S_{Mic} and $\delta^{13}C_{Pyro}$ are allowed to vary, which might arise because of changes in the C3:C4 ratio of pyrogenic precursor material[81], results in unrealistic changes to $\delta^{13}C_{Pyro}$.

Firn smoothing and isotopic disequilibrium. When CH_4 increases, atmospheric disequilibrium causes a depletion of $\delta^{13}C$–CH_4 and δD–CH_4 because sinks remove the lighter isotopologue faster[6,82,83]. Although this effect is incorporated into our one-box model analyses, we visualized its impact by running our model forward across the HE4–DO8 interval using S from equation (1) and constant isotopic sources signatures of −50‰ and −290‰ for $\delta^{13}C$–CH_4 and δD–CH_4, respectively. For $\delta^{13}C$–CH_4, this effect is small (at most 0.2‰) relative to observed variability (Extended Data Fig. 3b). Owing to stronger sink fractionation, the effect is more pronounced for δD–CH_4 (up to 8‰) and is comparable in magnitude to observed variability across HE4 and DO8 (Extended Data Fig. 3c). However, the true rate of CH_4 change may have been 50% higher than what is captured by WDC because of the smoothing effects of the firn column[9,64], causing our box model to underestimate the atmospheric disequilibrium effect by up to 50%. The largest disequilibrium effect for $\delta^{13}C$–CH_4 in our box model is 0.2‰, so it may be underestimated by at most 0.1‰. This is below our reported analytical precision and does not notably affect our analyses.

Because the amplitude of the atmospheric CH_4 pulses observed in WDC during HEs may be smoothed, it is likely that the pyrogenic emission pulses were larger in amplitude and shorter in duration than what is captured in our box model. Within each HE interval, box-modelled annual pyrogenic emissions increase by a maximum of 6–10 Tg yr^{-1} (Fig. 1c). Assuming the amplitude of the HE CH_4 pulses were dampened by 33% in WDC[9], we estimate that the true maximum increase in annual pyrogenic emissions during HEs was 9–15 Tg yr^{-1} (Extended Data Table 2). Because the CH_4 changes during DO events were stepwise, firn smoothing minimally affects modelled pyrogenic emission variability. To calculate the per cent change in global pyrogenic emissions (main text), we assume that baseline glacial CH_4 pyrogenic emissions were 10 Tg yr^{-1}, in line with the estimates from modelling studies[15,42,84,85]. Note that the absolute value of our per cent change estimates is highly sensitive to this baseline estimate and uncertainties related to firn smoothing[9]. Although firn processes dampen the amplitude of HE CH_4 pulses, the integrated magnitude of the CH_4 pulse is fully captured in WDC. We, therefore, estimate that pyrogenic pulses across each HE released 438–739 Tg of CH_4 over the course of 100–250 years, depending on the HE (Extended Data Table 2).

Latitudinal shifts in sources. Latitudinal shifts in CH_4 emissions affect the mean age of atmospheric CH_4 at ice core sites and thus measured $\delta^{13}C$–CH_4 and δD–CH_4 because of sink fractionation[4,6,21]. These shifts are tracked by the past relative interpolar difference (rIPD):

$$\text{rIPD} = \left(\frac{CH_{4,N}}{CH_{4,S}} - 1\right) \times 100\% \quad (11)$$

where $CH_{4,N}$ is NH CH_4 and $CH_{4,S}$ is SH CH_4 (ref. 86). For example, northward shifts of CH_4 emissions increase the age of atmospheric CH_4 in the SH, resulting in positive isotopic shifts over Antarctica that are not reflective of changes in source mixture. This effect was explored using a two-box model framework[6] with an interhemispheric exchange rate of 1 year (ref. 87). For both $\delta^{13}C$–CH_4 and δD–CH_4, the model was run forward with different ratios of NH to SH emissions but equal source signatures and sink fractionation factors from zero atmospheric burden to equilibrium. The results are plotted with NH and SH CH_4 isotopic signatures as a function of the resulting rIPD (Extended Data Fig. 4).

Based on constraints from existing ice-core-derived CH_4 rIPD data[36,71], we find that this mechanism would have affected Antarctic $\delta^{13}C$–CH_4 by at most 0.2‰. Specifically, ice core records suggest that the rIPD was about

3 percentage points higher during DO interstadials than stadials[11,24,70], which would have minimally impacted Antarctic $\delta^{13}C-CH_4$ (<0.1‰ at DO onsets) and our box model interpretations. HE-related CH_4 changes are too short in duration to accurately measure the rIPD (ref. 36), although we suspect that rIPD-induced $\delta^{13}C-CH_4$ changes were also small. The effect is more pronounced for $\delta D-CH_4$ (up to 8‰), which is comparable to the magnitude of observed $\delta D-CH_4$ variability (Extended Data Fig. 4).

CO_2 modelling

The 14-box ocean, atmosphere, and terrestrial biosphere carbon cycle model described in refs. 7,49 contains physical and biogeochemical constraints that realistically simulate interactions and lags in the carbon cycle. The model is ideal for testing how multiple components of the carbon cycle can combine to modulate atmospheric CO_2, without the added complexity and assumptions of more computationally expensive earth system models. The baseline scenario presented here (Fig. 4) was previously derived by forcing the model with climate records from Greenland and Antarctica, greenhouse gas forcing calculated from ice core gas records and Pa/Th records from the Bermuda Rise as proxies for AMOC strength[7,49]. The strength of each forcing was varied in a Monte Carlo approach to best match ice core CO_2 and $\delta^{13}-CO_2$ data over the past 65,000 years. We use this best-fit scenario as a baseline to perform our experiments, which test how the addition of BB fluxes may have contributed to some of the abrupt, enigmatic features of the CO_2 record that were not previously captured in the model.

Estimates of CO_2:CH_4 pyrogenic emission ratios were used to calculate CO_2 emissions from our box-modelled CH_4 emissions[88]. Because we report pyrogenic CH_4 emissions as relative change, we estimated total pyrogenic emissions by uniformly adjusting the HE5, HE4 and HE1 time series to initialize at 10 Tg yr^{-1}. CO_2:CH_4 emission ratios are well-characterized by modern observations but differ among ecosystems and fire regimes[88–90]. Uncertainties in tropical and mid-latitude vegetation and where burning occurred across HEs and DO events[32] limit our ability to pinpoint past CO_2:CH_4 emission ratios. We thus conservatively use a range derived from the mean and standard deviation of annual global emission ratios (125–170 gC gCH_4^{-1} from 1997 to 2022)[89,90].

The resulting time series of pyrogenic CO_2 emissions were incorporated into the carbon cycle model as a terrestrial flux to the atmosphere with a $\delta^{13}C-CO_2$ of −24‰. Following the pulses of increased BB, carbon stocks return to pre-pulse levels by imposing increases in ecosystem productivity with a 10–100-year e-folding timescale to represent the regrowth of ecosystems ranging from shrubland to mature forest. Uncertainties in pyrogenic CO_2 emissions and regrowth timescales were incorporated into the model assuming a 1,000-iteration Monte Carlo approach. The model was run from 65 kyr to 10 kyr with pyrogenic CO_2 emissions held constant between intervals for which estimates were available to ensure model equilibration (Fig. 4).

Several uncertainties are not incorporated into our model that could influence estimates of the impact of BB on atmospheric CO_2. First, although we incorporate absolute source signature and atmospheric $\delta^{13}C-CH_4$ uncertainties into our one-box model, uncertainties related to temporal variability in source signature (Fig. 3 and Extended Data Fig. 2) are not included (see sensitivity tests). Specifically, if the observed $\delta^{13}C-CH_4$ enrichments were partially driven by increases in microbial CH_4 emissions derived from ^{13}C-enriched C4 precursor biomass, modelled pyrogenic CH_4 and thus CO_2 emissions may be overestimated during HEs and DO events. Second, we assume that all terrestrial carbon combusted and emitted to the atmosphere is eventually regrown. However, the regional aridification induced by abrupt shifts in precipitation may have resulted in lower carbon biomass in newly established, post-fire ecosystems during HEs and DO events[32]. Carbon may have accumulated in regions in which precipitation increased, although terrestrial carbon loss in the drying, land-dominated NH tropics probably outweighed gains in the moister SH tropics during HEs[30,32,51,52]. The opposite was probably true during DO interstadials, with carbon uptake in the NH tropics from increased precipitation exceeding carbon loss in the land-limited SH tropics and leading to net terrestrial carbon uptake not captured by our model[30,32,91] (Extended Data Fig. 5). To prevent the over-parameterization of the model with poorly constrained variables, attempts to quantify terrestrial carbon fluxes other than those from BB emissions were not included outside of Extended Data Fig. 5, but their discussion is important for model interpretation.

At the peak of HE4 and HE1, our model indicates a 0.75–1.70 Pg yr^{-1} increase in pyrogenic carbon emissions. Assuming the amplitude of the approximately 150-year HE pyrogenic pulses were dampened by 33% in WDC[9] (see above), the true maximum pyrogenic carbon emission increase more likely ranged from 1.12 Pg $yr^{-1}$to 2.55 Pg yr^{-1}. Using the global mean modern ratio of 4 tonnes of carbon per hectare of burned area[90], we estimate that 285–637 million more hectares were burnt each year globally during HEs. This rough approximation is sensitive to the type of vegetation burned[92] but helps to conceptualize the geographic extent of the enhanced BB implied by our $\delta^{13}C-CH_4$ record.

Data availability

The WDC $\delta^{13}C-CH_4$ data measured on the OSU analytical system across HE5, DO12 and HE1 are publicly available and archived at the USAP DC (https://doi.org/10.15784/601683) and the NOAA National Climatic Data Center (https://www.ncei.noaa.gov/access/paleo-search/study/39699). The WDC $\delta^{13}C-CH_4$ data and $\delta D-CH_4$ data and the TALDICE $\delta D-CH_4$ measured at the University of Bern across HE4 and DO8 are publicly available on the USAP DC (TALDICE $\delta D-CH_4$: https://www.usap-dc.org/view/dataset/601814; WDC $\delta^{13}C-CH_4$ and $\delta D-CH_4$: https://www.usap-dc.org/view/dataset/601813) and the NOAA National Climatic Data Center (TALDICE $\delta D-CH_4$ and WDC $\delta^{13}C-CH_4$ and $\delta D-CH_4$: https://www.ncei.noaa.gov/access/paleo-search/study/39699). Box model and carbon-cycle model outputs are publicly available at Zenodo (https://doi.org/10.5281/zenodo.13974600; ref. 93) and can be found in the source data figure files associated with the online version of this paper. Source data are provided with this paper.

Code availability

The code used to run the methane isotope box model and plot the results in main text Figs. 1–4 is archived and publicly available at GitHub (https://github.com/benryoung23/Riddell-Young_etal_2024v2). The entire suite of Monte Carlo simulations and box model code used for the carbon cycle model simulations is publicly available at Zenodo (https://doi.org/10.5281/zenodo.13861216; ref. 94).

60. Schmitt, J., Seth, B., Bock, M. & Fischer, H. Online technique for isotope and mixing ratios of CH_4, N_2O, Xe and mixing ratios of organic trace gases on a single ice core sample. *Atmos. Meas. Tech.* **7**, 2645–2665 (2014).
61. Bock, M., Schmitt, J., Beck, J., Schneider, R. & Fischer, H. Improving accuracy and precision of ice core $\delta D(CH_4)$ analyses using methane pre-pyrolysis and hydrogen post-pyrolysis trapping and subsequent chromatographic separation. *Atmos. Meas. Tech.* **7**, 1999–2012 (2014).
62. Lee, J. E. *Interpreting Climate of the Past from High-Resolution Ice Core Records of Methane.* PhD thesis, Oregon State Univ. (2018).
63. Sigl, M. et al. The WAIS Divide Deep Ice Core WD2014 chronology – Part 2: annual-layer counting (0–31 ka BP). *Clim. Past* **12**, 769–786 (2016).
64. Schwander, J., Stauffer, B. & Sigg, A. Air mixing in firn and the age of the air at pore close-off. *Ann. Glaciol.* **10**, 141–145 (1988).
65. Sowers, T., Bender, M., Raynaud, D. & Korotkevich, Y. S. $\delta^{15}N$ of N_2 in air trapped in polar ice: a tracer of gas transport in the firn and a possible constraint on ice age–gas age differences. *J. Geophys. Res. Atmos.* **97**, 15683–15697 (1992).
66. Buizert, C., Sowers, T. & Blunier, T. Assessment of diffusive isotopic fractionation in polar firn, and application to ice core trace gas records. *Earth Planet. Sci. Lett.* **361**, 110–119 (2013).
67. Seierstad, I. K. et al. Consistently dated records from the Greenland GRIP, GISP2 and NGRIP ice cores for the past 104 ka reveal regional millennial-scale δ18O gradients with possible Heinrich event imprint. *Quat. Sci. Rev.* **106**, 29–46 (2014).
68. Lan, X. et al. Improved constraints on global methane emissions and sinks using $\delta^{13}C-CH_4$. *Global Biogeochem. Cycles* **35**, e2021GB007000 (2021).
69. Schwietzke, S. et al. Upward revision of global fossil fuel methane emissions based on isotope database. *Nature* **538**, 88–91 (2016).

70. Baumgartner, M. et al. High-resolution interpolar difference of atmospheric methane around the Last Glacial Maximum. *Biogeosciences* **9**, 3961–3977 (2012).
71. Beck, J. et al. Bipolar carbon and hydrogen isotope constraints on the Holocene methane budget. *Biogeosciences* **15**, 7155–7175 (2018).
72. Levine, J., Wolff, E., Hopcroft, P. O. & Valdes, P. J. Controls on the tropospheric oxidizing capacity during an idealized Dansgaard-Oeschger event, and their implications for the rapid rises in atmospheric methane during the last glacial period. *Geophys. Res. Lett.* **39**, L12805 (2012).
73. Saueressig, G. et al. Carbon 13 and D kinetic isotope effects in the reactions of CH_4 with $O(^1D)$ and OH: new laboratory measurements and their implications for the isotopic composition of stratospheric methane. *J. Geophys. Res. Atmos.* **106**, 23127–23138 (2001).
74. Sowers, T. Atmospheric methane isotope records covering the Holocene period. *Quat. Sci. Rev.* **29**, 213–221 (2010).
75. van Herpen, M. M. et al. Photocatalytic chlorine atom production on mineral dust–sea spray aerosols over the North Atlantic. *Proc. Natl Acad. Sci. USA* **120**, e2303974120 (2023).
76. Schüpbach, S. et al. Greenland records of aerosol source and atmospheric lifetime changes from the Eemian to the Holocene. *Nat. Commun.* **9**, 1476 (2018).
77. Lambert, F., Bigler, M., Steffensen, J. P., Hutterli, M. & Fischer, H. Centennial mineral dust variability in high-resolution ice core data from Dome C, Antarctica. *Clim. Past* **8**, 609–623 (2012).
78. Whitehill, A. R. et al. Clumped isotope effects during OH and Cl oxidation of methane. *Geochim. Cosmochim. Acta* **196**, 307–325 (2017).
79. Whiticar, M. J. & Faber, E. Methane oxidation in sediment and water column environments—isotope evidence. *Org. Geochem.* **10**, 759–768 (1986).
80. Etiope, G., Milkov, A. V. & Derbyshire, E. Did geologic emissions of methane play any role in Quaternary climate change? *Global Planet. Change* **61**, 79–88 (2008).
81. Randerson, J. et al. Fire emissions from C_3 and C_4 vegetation and their influence on interannual variability of atmospheric CO_2 and $\delta^{13}CO_2$. *Global Biogeochem. Cycles* **19**, GB2019 (2005).
82. Cantrell, C. A. et al. Carbon kinetic isotope effect in the oxidation of methane by the hydroxyl radical. *J. Geophys. Res. Atmos.* **95**, 22455–22462 (1990).
83. Schaefer, H. et al. Ice record of $\delta^{13}C$ for atmospheric CH_4 across the Younger Dryas-Preboreal transition. *Science* **313**, 1109–1112 (2006).
84. Hopcroft, P. O., Valdes, P. J. & Kaplan, J. O. Bayesian analysis of the glacial-interglacial methane increase constrained by stable isotopes and earth system modeling. *Geophys. Res. Lett.* **45**, 3653–3663 (2018).
85. Valdes, P. J., Beerling, D. J. & Johnson, C. E. The ice age methane budget. *Geophys. Res. Lett.* **32**, L02704 (2005).
86. Chappellaz, J. et al. Changes in the atmospheric CH_4 gradient between Greenland and Antarctica during the Holocene. *J. Geophys. Res. Atmos.* **102**, 15987–15997 (1997).
87. Mischler, J. A. et al. Carbon and hydrogen isotopic composition of methane over the last 1000 years. *Global Biogeochem. Cycles* **23**, GB4024 (2009).
88. Andreae, M. O. Emission of trace gases and aerosols from biomass burning – an updated assessment. *Atmos. Chem. Phys.* **19**, 8523–8546 (2019).
89. van Marle, M. J. et al. Historic global biomass burning emissions for CMIP6 (BB4CMIP) based on merging satellite observations with proxies and fire models (1750–2015). *Geosci. Model Dev.* **10**, 3329–3357 (2017).
90. van der Werf, G. R. et al. Global fire emissions estimates during 1997–2016. *Earth Syst. Sci. Data* **9**, 697–720 (2017).
91. Jochum, M. et al. Carbon fluxes during Dansgaard–Oeschger events as simulated by an Earth system model. *J. Clim.* **35**, 5745–5758 (2022).
92. Harrison, M. E., Page, S. E. & Limin, S. H. The global impact of Indonesian forest fires. *Biologist* **56**, 156–163 (2009).
93. Riddell-Young, B. Figure source data for Riddell-Young et al., 2024 "Abrupt changes in biomass burning during the last glacial period" (v.1). *Zenodo* https://doi.org/10.5281/zenodo.13974600 (2024).
94. Bauska, T. Carbon cycle model and analysis for Riddell-Young et al., 2024 "Abrupt changes in biomass burning during the last glacial period". *Zenodo* https://doi.org/10.5281/zenodo.13861216 (2024).
95. Riddell-Young, B. et al. Atmospheric methane variability through the Last Glacial Maximum and deglaciation mainly controlled by tropical sources. *Nat. Geosci.* **16**, 1174–1180 (2023).
96. Fujita, R. et al. Global and regional CH_4 emissions for 1995–2013 derived from atmospheric CH_4, $\delta^{13}C$–CH_4, and δD–CH_4 observations and a chemical transport model. *J. Geophys. Res. Atmos.* **125**, e2020JD032903 (2020).
97. Stell, A. C., Douglas, P. M., Rigby, M. & Ganesan, A. L. The impact of spatially varying wetland source signatures on the atmospheric variability of δD–CH_4. *Philos. Trans. R. Soc. A* **379**, 20200442 (2021).

Acknowledgements This work was supported by the US National Science Foundation award no. 1745078 and the M. J. Murdock Charitable Trust. The University of Bern acknowledges financial support from the Swiss National Science Foundation award no. 200020_172506 (R.I., J.S. and H.F.) and 200020B_200328L (J.S. and H.F.). We thank the National Science Foundation Ice Core Facility for their curation and preparation of the WAIS Divide Ice Core samples used in this study.

Author contributions Methane isotope data were measured by B.R.-Y., J.L., R.I., J.S. and H.F. Calibration and methods development of the OSU methane isotope system were done by B.R.-Y., J.A.M., E.J.B. and J.R.C. Box model analysis was carried out by B.R.-Y. and E.J.B. Carbon cycle box model analysis was done by B.R.-Y. and T.B. All authors contributed to the final paper.

Competing interests The authors declare no competing interests.

Additional information

Supplementary information The online version contains supplementary material available at https://doi.org/10.1038/s41586-024-08363-3.

Correspondence and requests for materials should be addressed to Ben Riddell-Young.

Peer review information *Nature* thanks Paul Lincoln, Vasilii Petrenko and the other, anonymous, reviewer(s) for their contribution to the peer review of this work. Peer reviewer reports are available.

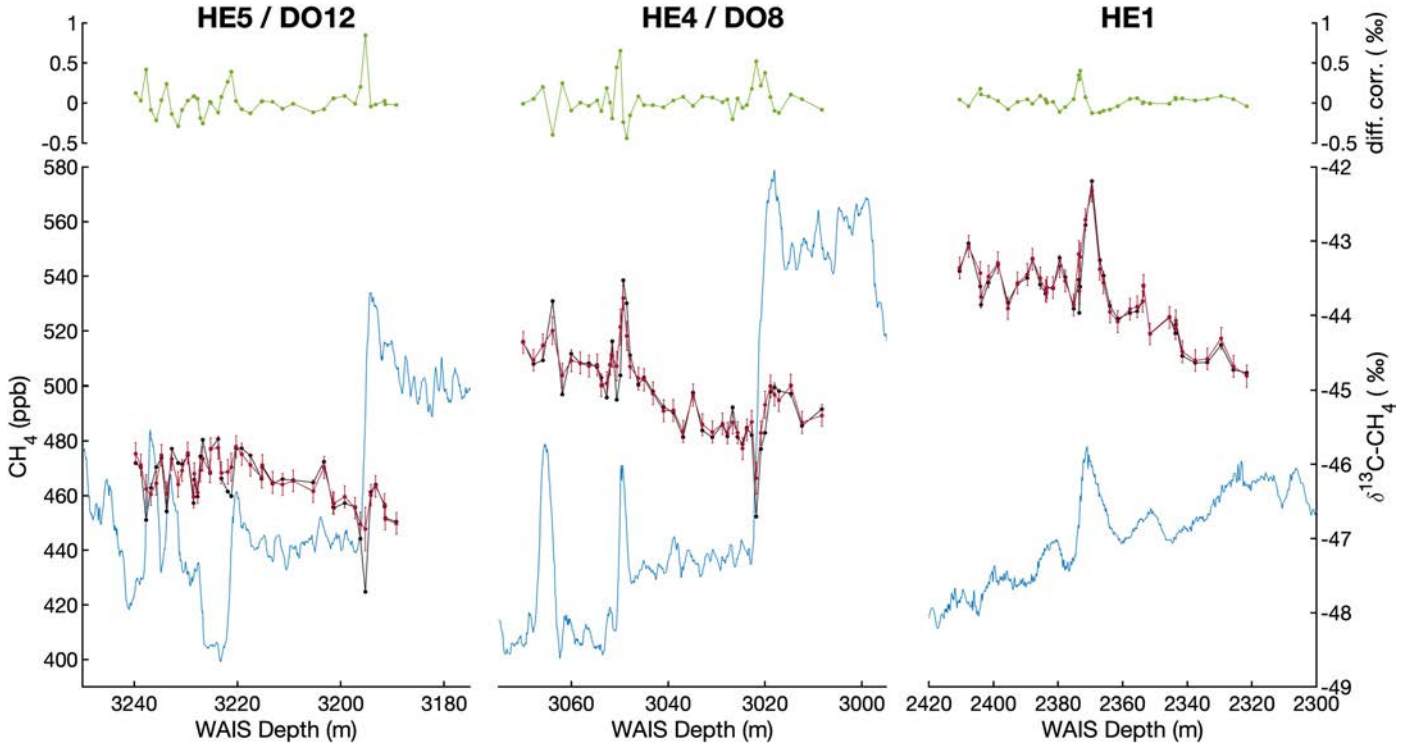

Extended Data Fig. 1 | Raw and fractionation-corrected $\delta^{13}C$–CH_4 data. Gravitational fractionation-corrected $\delta^{13}C$–CH_4 data (black) and gravitational and diffusional corrected $\delta^{13}C$–CH_4 data (maroon) for HE5/DO12 (left), HE4/DO8 (middle) and HE1 (right) plotted on the WAIS Divide depth scale. One-sigma analytical uncertainties, calculated using measurements precision and uncertainties related to the fractionation corrections, are plotted as maroon error bars for each data point. The WDC CH4 CFA record is plotted in light blue in each subplot[1]. The diffusional correction is plotted above in green for each data point.

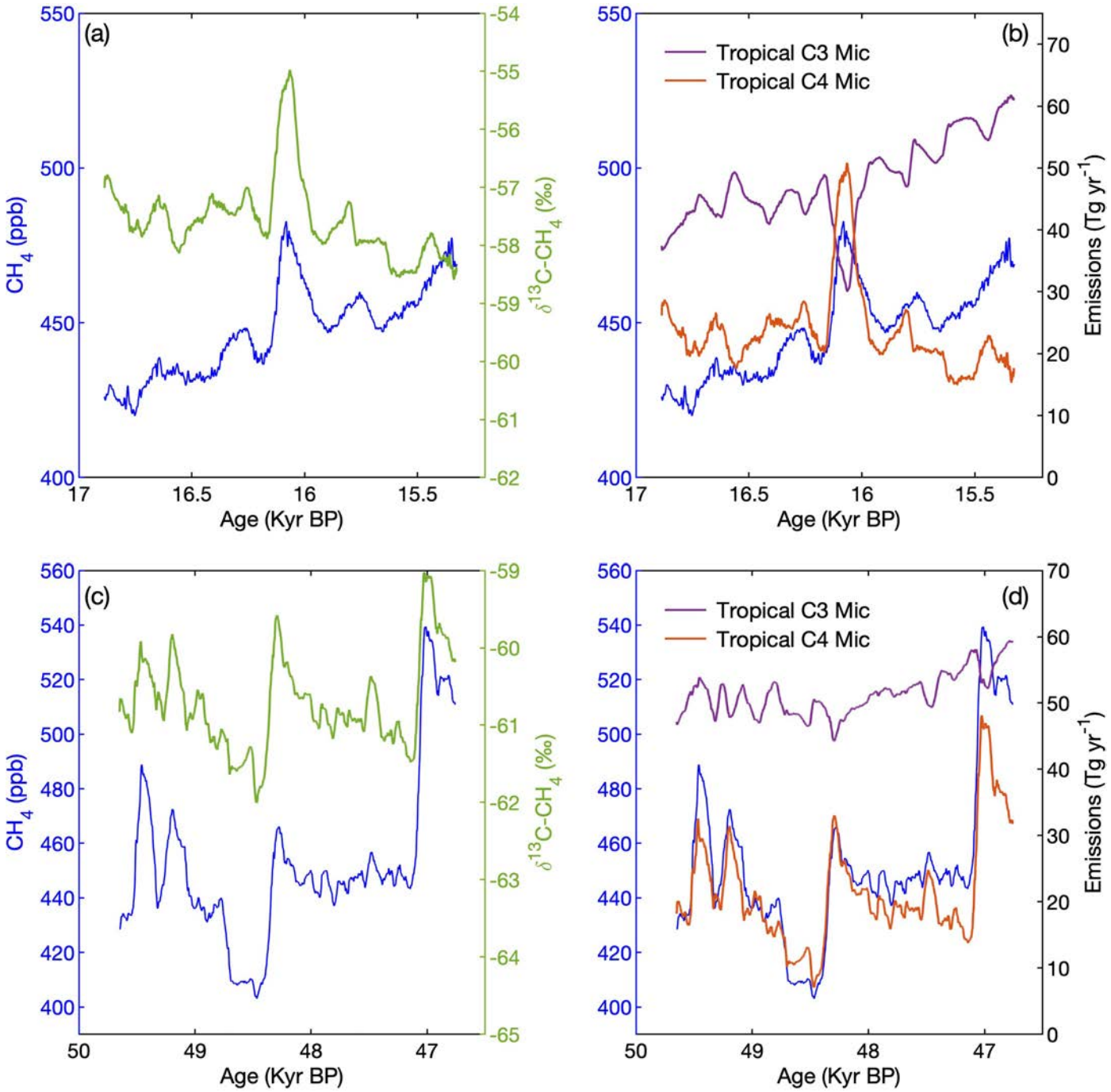

Extended Data Fig. 2 | Sensitivity tests for HE5/DO12 and HE1 datasets. Modelled microbial $\delta^{13}C-CH_4$ assuming constant pyrogenic and geologic $\delta^{13}C-CH_4$ and emissions for (a) HE1 and (c) HE5/DO12. Calculated emission strength of microbial CH_4 emissions derived from C3-dominant (green) or C4-dominant (orange) precursor biomass from the tropical regions using the results of the lefthand panels for (b) HE1 and (d) HE5/DO12. The WDC CFA record is shown in blue in each subplot[1].

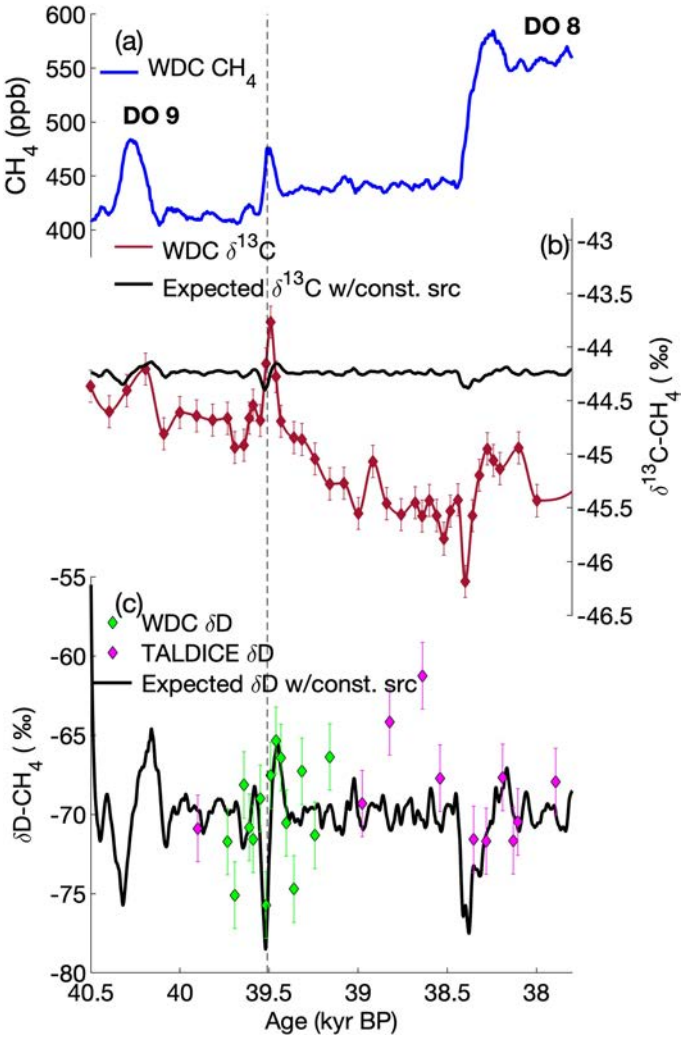

Extended Data Fig. 3 | Atmospheric disequilibrium effect for δD–CH_4 and δ^{13}C–CH_4. (a) WDC CH_4 CFA data (blue)[1,53]. (b) Measured δ^{13}C–CH_4 data (red diamonds) plotted with 1-sigma measurement uncertainties and spline-interpolated to the resolution of the CFA CH_4 data (red). Modelled atmospheric δ^{13}C–CH_4 assuming constant δ^{13}C–CH_4 of the global source (black) to visualize the impact of atmospheric disequilibrium on δ^{13}C–CH_4. (c) Measured δD–CH_4 data plotted with 1-sigma uncertainties from WDC (green diamonds) and TALDICE (magenta diamonds) plotted on the WDC-synchronized gas age scale from[57,58]. Modelled atmospheric δD–CH_4 assuming constant δD–CH_4 of the global source (black) to visualize the impact of atmospheric disequilibrium on δD–CH_4. The onset of HE4 is indicated by a vertical dashed line.

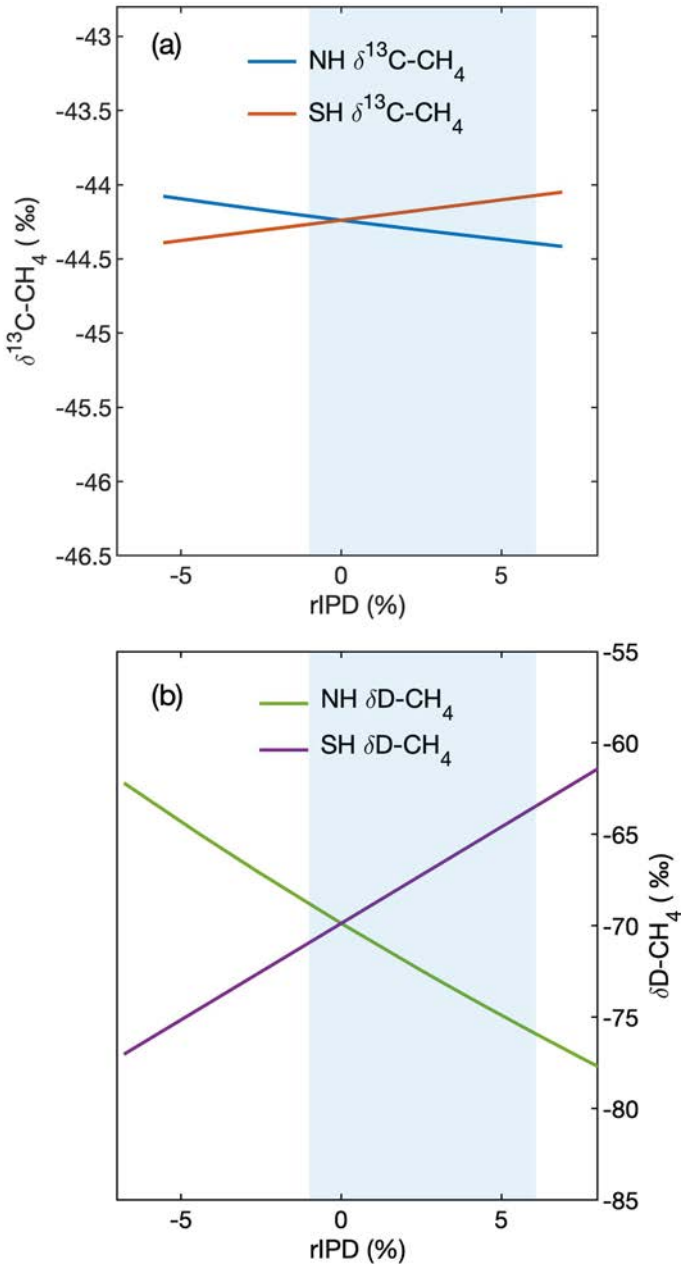

Extended Data Fig. 4 | Two-box model sensitivity tests. Two-box model equilibrium for (a) δ^{13}C-CH$_4$ and (b) δD-CH$_4$ for scenarios with varying latitudinal source distribution (indicated by the x-axis: rIPD), but the same isotopic source signature. Varying latitudinal source distribution is displayed on the x-axis as the rIPD, which is the percent difference in NH and SH atmospheric CH$_4$ mixing ratio[11,25,70,95]. The range of observed rIPD values indicated by ice core studies are shaded in blue. (a) δ^{13}C-CH$_4$ for the NH (green) and SH (purple) are shown as a function of rIPD. (b) δD-CH$_4$ for the NH (green) and SH (purple) are also shown as a function of rIPD. The equilibrium isotopic composition was calculated using a two-box model with prescribed hemispheric source signatures (methods)[6].

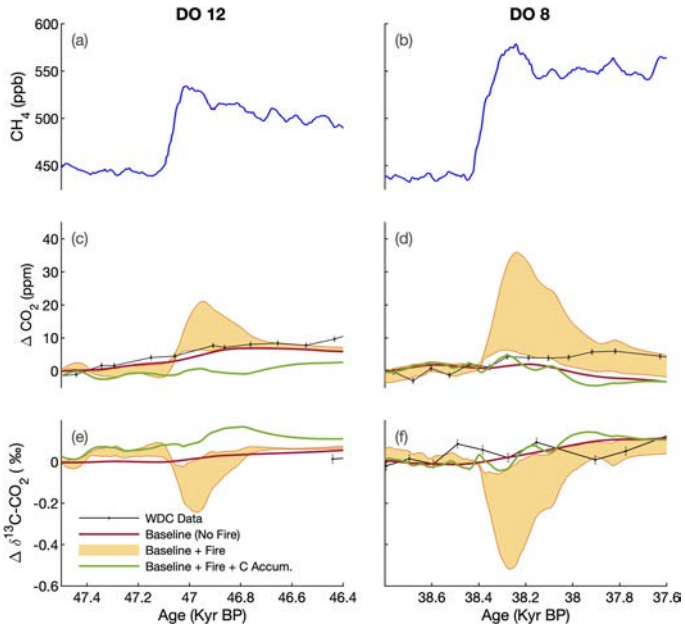

Extended Data Fig. 5 | Modelled CO_2 change during DO Events. Same as main text Fig. 4 but showing carbon cycle box-model results for DO12 (left) and DO8 (right) and including model results with changes to NPP associated with abrupt climate events (green). Changes to terrestrial carbon uptake due to changes in primary productivity were calculated using our one-box modelled microbial CH_4 emissions as a proxy for terrestrial carbon storage with a theoretical conversion factor of 1 Tg of microbial CH_4 emissions per 8 Pg of carbon stocks. Our modelled increases in terrestrial carbon stock at the onset DO Interstadials cancel carbon losses implied by the modelled pyrogenic CO_2 emissions and are consistent with earth system modelling studies[15,32,52,91]. These studies similarly attribute the increase in terrestrial carbon to enhanced productivity associated with greater moisture availability over the land-dominated NH tropics.

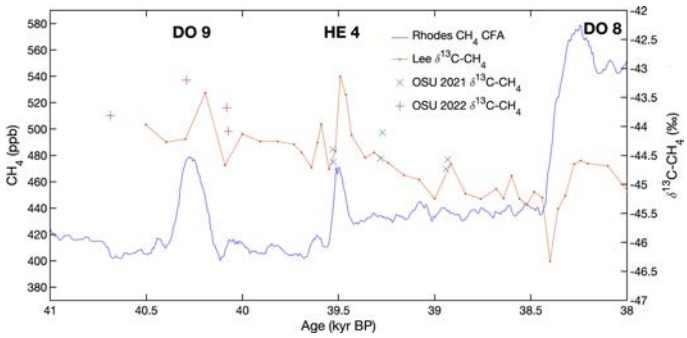

Extended Data Fig. 6 | Comparison of OSU and Bern $\delta^{13}C-CH_4$ data across HE4, DO8 and DO9 from the WDC ice core. WDC CFA CH_4 data (left axis, blue line)[1,53], $\delta^{13}C-CH_4$ measured by James Lee at the Bern (orange), OSU $\delta^{13}C-CH_4$ measurements made in 2021 prior to the H1 WDC measurement campaign (light blue Xs), and OSU $\delta^{13}C-CH_4$ measurements made in 2022 prior to the HE5/DO12 measurement campaign (maroon +s). Data are not corrected for gravitational or diffusive firn fractionation, which allows for direct comparison between the $\delta^{13}C-CH_4$ that is trapped in the ice sample.

Extended Data Table 1 | Stable isotope signatures used in the 1-box model output isotope mass balance[21,96]

CH_4 Source	$\delta^{13}C\text{-}CH_4$ (‰)	$\delta D\text{-}CH_4$ (‰)
Global Microbial (Mic)	-60 +/- 1.5	-318 +/- 13
Pyrogenic (Pyro)	-22 +/- 1.8	-211 +/- 15
Geologic (Geo)	-44 +/- 0.4	-197 +/- 10
C3-dominant Microbial (C3)	-60 +/- 1.5	-
C4-dominant Microbial (C4)	-50 +/- 1.5	-
High-Lat NH Microbial (Hl)	-68 +/- 3.1	-

One-sigma uncertainties for $\delta^{13}C$ and δD source signatures from[21] were incorporated into our box model output uncertainty. The $\delta^{13}C\text{-}CH_4$ emitted from C3- and C4-dominant biomass, the high-latitude NH microbial source $\delta^{13}C\text{-}CH_4$, and one-sigma uncertainties were obtained from[97]. Parentheses denote the subscripts used in Eqs. 1–10 (methods).

Extended Data Table 2 | Summary of the magnitude of the pyrogenic pulses associated with HE5, 4 and 1

Heinrich Event	Box-model max annual increase (Tg yr^{-1})	Est. max annual increase (Tg yr^{-1})	Pyrogenic Pulse Duration (yr)	Total pyrogenic pulse emissions (Tg)	1-sigma Unc. (Tg)	Avg. emission rate (Tg yr^{-1})
HE5	6	9	250	501	196	2.0
HE4	9	14	110	438	104	4.0
HE1	10	15	180	739	154	4.1

From left to right: (1) The HE; (2) The box-modelled maximum annual increase in pyrogenic emissions from baseline values during each HE (Tg yr^{-1}); (3) The estimated true maximum annual increase based on the assumption of a 33% damping of the signal amplitude due to firn smoothing in WDC[9] (Tg yr^{-1}); (4) The duration of the CH_4 pulses associated with each HE (yr); (5) The integrated total anomalous pyrogenic CH_4 emissions across each HE (Tg); (6) The 1-sigma uncertainty of (5) (Tg); (7) The average annual increase in pyrogenic emissions (Tg yr^{-1}), calculated by dividing (5) by (4).